2008

Model for current drive stabilization of neoclassical tearing modes

Jennifer Woodby
Lehigh University

Woodby, Jennifer

Model for Current Drive Stabilization of Neoclassical Tearing Modes

May 2008

Model for Current Drive Stabilization of Neoclassical Tearing Modes

by

Jennifer Woodby

A Thesis
Presented to the Graduate and Research Committee
of Lehigh University
in Candidacy for the Degree of
Master of Science

in

Mechanical Engineering

Lehigh University

April 2008

Certificate of Approval

This thesis is accepted and approved in partial fulfillment of the requirements for the Master of Science.

4/22/08

Date

Thesis Advisor

Co-Advisor

Department Chair

Acknowledgements

I would like to thank my advisor, Professor Schuster, as well as Professors Bateman and Kritz for their guidance and support for my research. I would also like to thank Federico Halpern and Lixiang Luo for their help with Fortran and the ISLAND module. Lastly, I would like to thank Yongsheng Ou, Chao Xu, and Majed Alsarheed for their help with difficult coursework, and for keeping the lab entertaining!

Contents

List of Figures

Abstract

A model derivation is presented for the effect of current drive on the saturated width of magnetic islands driven by the neoclassical tearing mode (NTM) instability in axisymmetric plasmas. The derivation is carried out for pulsed current that is driven at the same angle as the island O-point, as well as continuous current drive. The results of the derivation are implemented in the ISLAND module to compute saturated magnetic island widths. It is found that the greatest stabilizing effect of both pulsed and continuous current drive on the island width is achieved when current is driven at the radius of the island center. In addition, narrow current drive is more effective at stabilizing the magnetic islands than wide current drive for which more current falls outside the island. When pulsed and continuous current drives are compared for equal total driven current, the pulsed current is shown to be more effective, particularly as the offset from the island center increases.

Chapter 1

Introduction

1.1 Nuclear Fusion and the Tokamak

As fossil fuels begin to run out and world energy demand continues to increase, alternative energy sources will have to meet the predicted energy shortfall. The options include renewable sources such as solar, wind, or geothermal energy, which are attractive from an ecological viewpoint. However, none of these options provides sufficient energy density to realistically supply an increasingly urbanized world. Nuclear fission and fusion do provide sufficient energy density to meet world demands. Nuclear fission is widely used in nuclear power plants today, while fusion is not yet commercially available. The main problems with widespread nuclear fission facilities are the risk of nuclear accident and the problem of nuclear waste. These difficulties are avoided with nuclear fusion, which poses relatively little risk of nuclear accident and produces minimal radioactive waste. An additional advantage of nuclear fusion is its use of abundant

hydrogen isotopes from water for fuel.

Controlled fusion is extremely technologically challenging. Fusion occurs when the nuclei of two light atoms such as isotopes of hydrogen are fused together to form a heavier (helium) nucleus, producing energy as a by-product. Fusion is the reaction that fuels the sun and stars, where intense pressure causes the hydrogen and other light nuclei to fuse, producing heavier elements.

The tokamak (a Russian acronym for toroidal chamber with magnetic coils) is the most widely studied controlled fusion device today. In tokamaks, hydrogen plasma is confined magnetically. The pressure and temperature inside the device must be raised to extremely high levels for fusion to occur. Active control is necessary to produce and regulate plasmas with sufficient density, temperature, and confinement. Under these conditions, there are several instabilities that can lead to plasma disruption if they are not controlled. This thesis focuses on the neoclassical tearing mode instability and its control via localized current drive.

1.2 Control of the NTM Instability

The neoclassical tearing mode (NTM) instability produces magnetic islands which can degrade confinement and lead to plasma disruptions in tokamak plasmas. The central physical process that drives NTMs is the bootstrap current density, which is driven by the plasma pressure gradient outside of magnetic islands and is nearly absent inside magnetic islands, where the pressure profile is locally flattened. The lack of bootstrap current within each island produces a helical perturbation in the total current density,

which enhances the NTM instability and increases the resulting magnetic island widths. NTMs can be stabilized by driving current locally within each magnetic island in order to replace the missing bootstrap current density. A model for the stabilization of NTMs by localized current drive is derived in this thesis.

The magnetic islands produced by NTMs have been observed in tokamak experiments [1, 2, 3]. As tokamaks operate with higher pressure and longer pulse lengths, NTMs become more deleterious. The most damaging magnetic islands are those with low poloidal and toroidal mode numbers, e.g. $m/n = 2/1,\ 3/2$, where m is the poloidal mode number (the short way around the tokamak) and n is the toroidal mode number (the long way around the tokamak). Since NTMs are stable for sufficiently small magnetic island widths, a "seed" perturbation is required in order to start NTM island growth. Hence, in general, NTMs are linearly stable and nonlinearly unstable. For stabilization it is therefore sufficient to shrink the islands to a critical width below which they continue to shrink on their own.

In recent years, considerable progress has been made in the physics [2] and control of NTMs [4], and today several techniques are available to suppress NTMs and maintain stability. Strategies to avoid and suppress NTMs [3] include: (1) reducing or eliminating noise from other instabilities in order to keep the NTM seed islands sufficiently small, (2) using helical fields from other, benign, modes or externally applied fields to inhibit the perturbed bootstrap currents of modes of concern, or (3) applying radio frequency (rf) power current drive (e.g. electron cyclotron current drive, ECCD [5]) parallel to the equilibrium plasma current at mode rational surfaces in order to increase the linear stability and replace the "missing" bootstrap current within magnetic

islands. The last of these stabilization methods — current drive within each magnetic — is the focus of this paper. The effect of localized current drive is modeled and implemented in the ISLAND module [7, 8] to compute the saturated magnetic island widths. The theory of tearing mode stabilization in toroidal plasmas by RF driven currents that are modulated in phase with the island rotation has been previously studied in [6]. In that paper, transient effects such as finite time response of the driven current are considered, and a dynamical model is developed. This paper considers only the steady state solution.

The ISLAND module in the National Transport Code Collaboration Module Library (http://w3.pppl.gov/NTCC) is an implementation of a quasi-linear model to compute magnetic island widths driven by saturated neoclassical tearing modes. The ISLAND module is intended to be used in axisymmetric toroidal plasmas with arbitrary aspect ratio, cross-sectional shape, and plasma beta. An adaptive ODE solver is used in a shooting method to integrate a coupled system of ODEs for harmonics of the magnetic perturbation, which are derived from the three-dimensional scalar plasma pressure force balance equations. An additional term representing the effects of localized current drive in the coupled system of ODEs in the ISLAND module is derived in this thesis.

In this thesis, the effect of localized current drive on the saturated widths of magnetic islands is investigated. In Chapter 2, the procedure for finding saturated magnetic island widths without current drive is outlined. In Chapter 3, a Gaussian current drive term is introduced, and the derivation of Chapter 2 is repeated for the resulting total current profile including the current drive. In Chapter 4, the mathematical differences

between pulsed current driven at the island O-point and continuously driven current are presented. In Chapter 5, the normalization procedure for the differential flux surface areas is explained. Chapter 6 illustrates the computation of total driven current in Amperes. Chapter 7 shows the results of implementation of localized current drive in the ISLAND module for both pulsed and continuous current drive profiles. Chapter 8 concludes the work.

Chapter 2

Finding Saturated Magnetic Island Widths

Following the derivation presented in [9], a system of ordinary differential equations can be derived for the solution of the three-dimensional, scalar pressure plasma equilibrium force-balance equations

$$\mathbf{J} \times \mathbf{B} = \nabla p \tag{2.1}$$

$$\nabla \times \mathbf{B} = \mu_0 \mathbf{J} \tag{2.2}$$

$$\nabla \cdot \mathbf{B} = 0 \tag{2.3}$$

where $\mathbf{J}$ is the current density, $\mathbf{B}$ is the magnetic field, p is the scalar pressure, and μ_0 is the permeability of free space. These equations are expressed in Hamada-like coordinates [9], where V is a flux surface label, θ is a poloidal angle-like variable, and ζ is a toroidal angle-like variable. A small perturbation about an axisymmetric equilibrium

field is applied ($\mathbf{B} = \mathbf{B}^0 + \mathbf{B}^1$, where the "0" superscript denotes the unperturbed axisymmetric field, "1" represents the first order perturbation) and corresponding perturbations are made to the current density $\mathbf{J}$ and the plasma pressure p. Equations (1)-(3) are expressed in terms of a combination of contravariant and covariant components. All perturbed variables X^1 are written as a series of Fourier harmonics of θ and ζ with the form,

$$X^1(V,\theta,\zeta) = \sum_{m,n} X^1_{mn}(V) \exp\left[i(m\theta - n\zeta)\right]. \tag{2.4}$$

The divergence-free property of the perturbation component of the magnetic field, $\nabla \cdot \mathbf{B}^1 = 0$, can then be written in terms of the contravariant components of $\mathbf{B}^1$ as [9]

$$\frac{d}{dV}(-i\mathcal{J}B^{1V}_{mn}) = n\mathcal{J}B^{1\zeta}_{mn} - m\mathcal{J}B^{1\theta}_{mn} \tag{2.5}$$

where $\mathcal{J} = (\nabla V \cdot \nabla\theta \times \nabla\zeta)^{-1}$ is the Jacobian of the axisymmetric coordinates, and the superscripts of V, ζ, θ indicate contravariance. After combining the other perturbation equations it can be shown that

$$\begin{aligned}(nB^{0\zeta} - mB^{0\theta})\left(\frac{d}{dV}B^1_{\theta mn} - imB^1_{Vmn}\right) \\ = \mu_0(nJ^{0\zeta} - mJ^{0\theta})\mathcal{J}B^{1\zeta}_{mn} - i\mathcal{J}B^{1V}_{mn}B^{0\zeta}\frac{d}{dV}\frac{\mu_0 J^{0\zeta}}{B^{0\zeta}} + m\mu_0 p^1_{mn}\frac{1}{B^{0\zeta}}\frac{d}{dV}B^{0\zeta}\end{aligned} \tag{2.6}$$

where the subscripts of V and θ indicate covariant components of the perturbed field.

Equations (2.5) and (2.6) form a coupled pair of ODEs for each helical harmonic of the variables $[-i\mathcal{J}B^{1V}_{mn}, B^1_{\theta mn}]$. Additional algebraic equations can be derived to close the set [9]. A flat spot in the normalized current density $\mu_0 J^{0\zeta}/B^{0\zeta}$ and the plasma pressure p is produced by the presence of a magnetic island at each mode rational surface which prevents the ODEs from being singular at mode rational surfaces, where

$nB^{0\zeta} - mB^{0\zeta} = 0$. An iterative algorithm is used for the determination of saturated tearing mode island widths as eigenvalues for the differential boundary value equations. Such an algorithm has been implemented in the iSLAND module [9]. The normalized current density term $\mu_0 J^{0\zeta}/B^{0\zeta}$ in Equation (2.6) is modified in this thesis to account for the effects of current drive.

A detailed derivation of the effect of magnetic islands on the axisymmetric averaged current density profile without current drive is presented first. A similar derivation applies to the pressure profile. The result of this derivation is given in [9].

Along a cut through the widest part of the island (where $\alpha \equiv m\theta - n\zeta = 0$), assume that the current density profile has the form

$$\frac{\mu_0 J^{\zeta}}{B^{\zeta}} \equiv K(u) = \begin{cases} K_0 + K_1(-1-u) & u < -1 \\ K_0 & |u| \leq 1 \\ K_0 + K_1(1-u) & u > 1 \end{cases} \tag{2.7}$$

where K_0 and K_1 are constants determined by the local current profile, H_{mn} is the island half-width, and $u \equiv (V - V_{mn})/H_{mn}$ is the normalized radial coordinate, measured from the island center (since V_{mn} is the V-location of the mode-rational surface).

When current density is driven at some point (u, α), the resulting current at any other point (u', α') can be found by exploiting the fact that current density is spread over surfaces of constant magnetic flux, as illustrated in Figure 2.1. Consider a function ψ which is uniform along magnetic field lines, so that

$$\mathbf{B} \cdot \nabla \psi = 0. \tag{2.8}$$

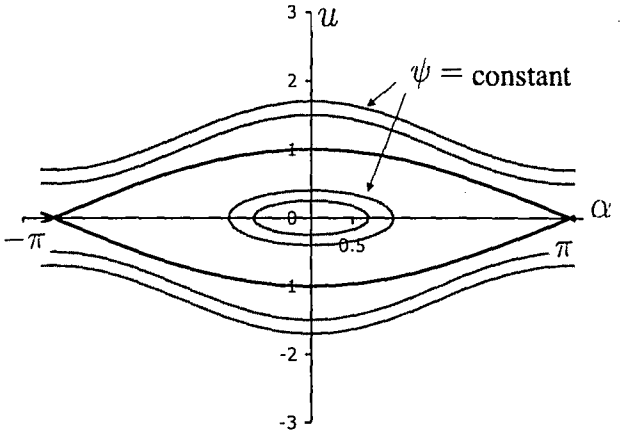

Figure 2.1: Surfaces of constant magnetic flux ψ

This function is expanded in a Taylor series in the neighborhood of the mode-rational surface, as in [10],

$$\psi = \psi^0_{mn} - 2\psi^1_{mn}u^2 + ... + \psi^1_{mn}\cos\alpha. \tag{2.9}$$

Equation (2.9) is solved for u in terms of ψ,

$$u = \pm\sqrt{\frac{\psi^0_{mn} + \psi^1_{mn}\cos\alpha - \psi}{2\psi^1_{mn}}} \tag{2.10}$$

which is then used in Equation (2.9) again (as $\psi = \psi^0_{mn} - 2\psi^1_{mn}u'^2 + ... + \psi^1_{mn}\cos\alpha'$) to determine the mapping from any point (u', α') to any other point (u, α) along a magnetic surface

$$u = \pm\sqrt{\frac{\cos\alpha - \cos\alpha' + 2u'^2}{2}}. \tag{2.11}$$

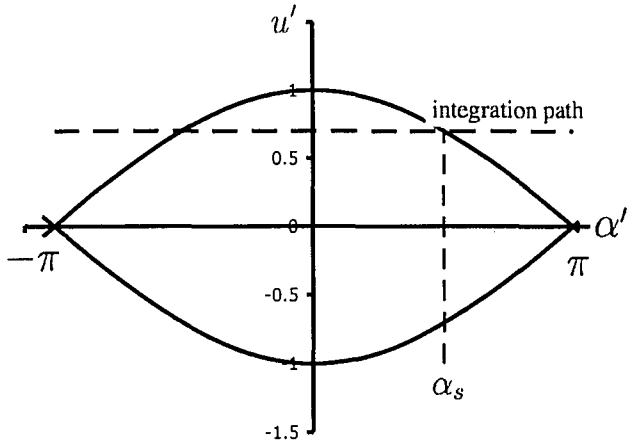

Figure 2.2: Sketch of Integration Path

In Equation (2.11), α represents the current drive location, and α' is the coordinate over which the axisymmetric average is computed. If the current is driven only at the widest part of the island, $\alpha = 0$, this expression simplifies to

$$u\big|_{\alpha=0} = \pm\sqrt{\frac{1-\cos\alpha'+2u'^2}{2}}. \tag{2.12}$$

One can then find the axisymmetric average current density $K^0 \equiv \mu_0 J^{0\zeta}/B^{0\zeta}$, which is used in Equation (2.6)

$$\begin{aligned} K^0(u') &= \frac{1}{2\pi}\int_{-\pi}^{\pi} K(u',\alpha')d\alpha' \\ &= \frac{1}{\pi}\int_{0}^{\pi} K(u',\alpha')d\alpha'. \end{aligned} \tag{2.13}$$

In Figure 2.2, it can be seen that the integration must be divided into two different regions — one region inside the island and one outside. Note also that the function

$K(u', \alpha')$ being integrated in Equation (2.13) changes with the sign of u': at the outboard side of the island, u' is positive (corresponding to the (+) sign in Equations (2.10)-(2.12)), while at the inboard side u' is negative (corresponding to the (−) sign). Nonetheless the derivative dK^0/dV is expected to be symmetric in u' when there is no current drive.

The value of α' at the separatrix is found by setting $\left|u\right|_{\alpha=0}\left| = 1\right.$ in Equation (2.12) and solving for α'

$$\begin{aligned} \alpha_s &= \cos^{-1}(2u'^2 - 1), \quad |u'| < 1 \\ &= \pi - 2\sin^{-1}[\min(1, |u'|)]. \end{aligned} \tag{2.14}$$

Expression (2.12) is used in Equation (2.7) and the integration (2.13) is carried out to obtain

$$\frac{\mu_0 J^{0\zeta}}{B^{0\zeta}} \equiv K^0 = \begin{cases} K_0 + \frac{K_1}{\pi}\left[-\alpha_s - 2\sqrt{1+u'^2}\,\mathrm{E}(\phi_m, \frac{1}{1+u'^2})\right] & u' > 0 \\ K_0 + \frac{K_1}{\pi}\left[\alpha_s - 2\sqrt{1+u'^2}\,\mathrm{E}(\phi_m, \frac{1}{1+u'^2})\right] & u' < 0 \end{cases} \tag{2.15}$$

where

$$\phi_m = \sin^{-1}\left[\min(1, |u'|)\right] \tag{2.16}$$

and $\mathrm{E}(\phi, m)$ is the incomplete elliptic integral of the second kind. (Note that in [9], the notation $\mathrm{E}(\phi, k)$ is used, where $k^2 \equiv m$.)

The derivative of this axisymmetric average current density results in

$$\begin{aligned}\frac{dK^0}{dV} &= -\frac{K_1}{\pi H_{mn}}\left\{\frac{2}{\sqrt{1-u'^2}} - \frac{2|u'|}{\sqrt{1+u'^2}}\,\mathrm{E}(\phi_m, \frac{1}{1+u'^2}) - \frac{2}{\sqrt{1-u'^2}}\right. \\ &\quad \left. + \frac{2|u'|}{\sqrt{1+u'^2}}\left[\mathrm{E}(\phi_m, \frac{1}{1+u'^2}) - \mathrm{F}(\phi_m, \frac{1}{1+u'^2})\right]\right\} \\ &= \frac{2K_1}{\pi H_{mn}}\frac{|u'|}{\sqrt{1+u'^2}}\mathrm{F}(\phi_m, \frac{1}{1+u'^2}) \qquad (2.17)\end{aligned}$$

where $\mathrm{F}(\phi, m)$ is the incomplete elliptic integral of the first kind. This result is used in Equation (2.6), which is then used to compute the saturated magnetic island widths.

Chapter 3

Current Drive with Gaussian Profile

If a localized current drive is added to the current profile through the widest part of the island given in Equation (2.7), there is an additional term for the current drive density, K_{EC}, which has components both inside and outside the island

$$\frac{\mu_0 J^\zeta}{B^\zeta} \equiv K(u) = \begin{cases} K_0 + K_1(-1-u) + K_{EC}(u) & u < -1 \\ K_0 + K_{EC}(u) & |u| < 1 \\ K_0 + K_1(1-u) + K_{EC}(u) & u > 1 \end{cases} \tag{3.1}$$

Here, the driven current density profile K_{EC} is assumed to have a Gaussian form as shown in Figure 3.1,

$$K_{EC}(u) = K_m \exp\left[\frac{-(u-a)^2}{2\sigma^2}\right] \tag{3.2}$$

where a is the offset, K_m is the maximum height, and σ is the variance.

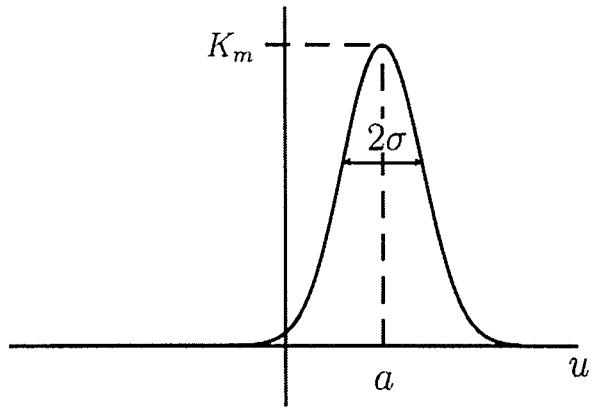

Figure 3.1: Sketch of current density $K_{EC}(u)$, where K_m is the maximum height, a is the offset, and σ is the variance

Since the terms in the current profile, Equation (3.1), are linear, and the first two terms in Equation (3.1) are the same as those in Equation (2.7), it is possible to consider the current drive term separately since all other terms will be unaffected. The shape of surfaces of constant magnetic flux ψ is shown in Figure 3.2. A Taylor series expansion is used for ψ near the mode rational surface as in Equation (2.9), and the expression can be solved for u as in (2.12).

Note that the height, width, and offset of the current drive are free parameters in Equation (3.2). For a centered Gaussian with a width on the order of the island width, this current drive shape is qualitatively similar to the parabolic current peaking factor introduced in [9], so the results for the Gaussian shape can be compared with results from the parabolic peaking factor model.

Although the current drive is limited to a narrow region near $\alpha = 0$, the current

spreads over the flux surfaces, and using Equation (2.11), Equation (3.2) becomes

$$K_{EC}(\psi) = K_m \exp\left[\frac{-1}{2\sigma^2}\left(\pm\sqrt{\frac{\cos\alpha - \cos\alpha' + 2u'^2}{2}} - a\right)^2\right]\left(\frac{dA}{dS}\right) \qquad (3.3)$$

The factor dA/dS results from the fact that the current applied to an area dA in u-coordinates is spread over an area dS in ψ-coordinates, as illustrated in Figure 3.2. In this expression, the angle α represents the current drive location and α' represents the angle over which the current density is spread. Note that current can be driven over any range of α, but in Chapter 4.1 it will be assumed that current is driven at $\alpha = 0$ only for pulsed current drive. Equation (3.3) is plotted in Figure 3.3 for $\alpha = 0$, an arbitrary peak value K_m, $\sigma = 0.2$, and $dA/dS = 1$.

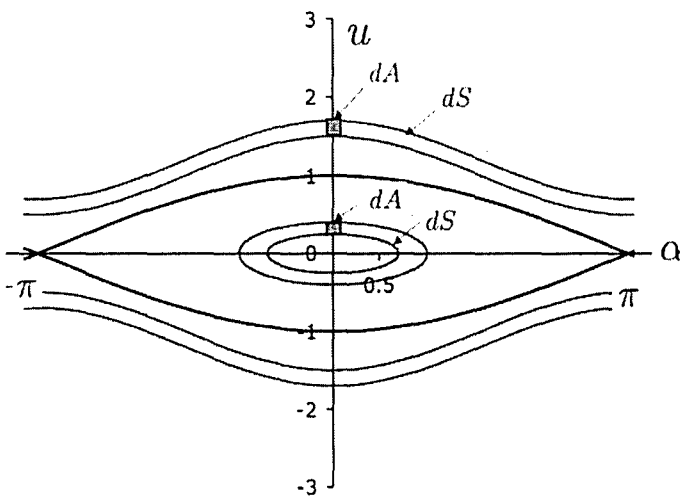

Figure 3.2: Shape of magnetic flux surfaces

Now the goal is to integrate Equation (3.3) over both α and α' to find the axisymmetric averaged current drive density. Then the derivative of this averaged current drive density, in addition to the derivative of the background current density, is used to

produce the $d(\mu_0 J^{0\varsigma}/B^{0\varsigma})/dV$ term required in Equation (2.6), which is used in the ISLAND module.

Direct integration of this current drive profile produces the expression

$$K^0_{EC} = \frac{1}{\pi}\int_0^{\pi}\int_{\alpha}^{\pi} K_{EC}(\psi)d\alpha' d\alpha \tag{3.4}$$

$$= \frac{K_m}{\pi}\left\{\int_0^{\alpha_s}\int_{\alpha}^{\alpha_s}\exp\left[\frac{-1}{2\sigma^2}\left(\pm\sqrt{\frac{\cos\alpha - \cos\alpha' + 2u'^2}{2}} - a\right)^2\right]\left(\frac{dA}{dS}\right)_{in} d\alpha' d\alpha\right.$$

$$\left. + \int_{\alpha_s}^{\pi}\int_{\alpha}^{\pi}\exp\left[\frac{-1}{2\sigma^2}\left(\pm\sqrt{\frac{\cos\alpha - \cos\alpha' + 2u'^2}{2}} - a\right)^2\right]\left(\frac{dA}{dS}\right)_{out} d\alpha' d\alpha\right\}$$

where the separatrix value α_s is defined in Equation (2.14), and $(dA/dS)_{in}$ and $(dA/dS)_{out}$ are the ratios of the area of the current drive relative to the area over which the current density spreads inside and outside the island. These differential area ratios will be discussed in detail in Chapter 5. Even if dA/dS is taken to be constant, the integrals of Equation (3.4) cannot be carried out analytically.

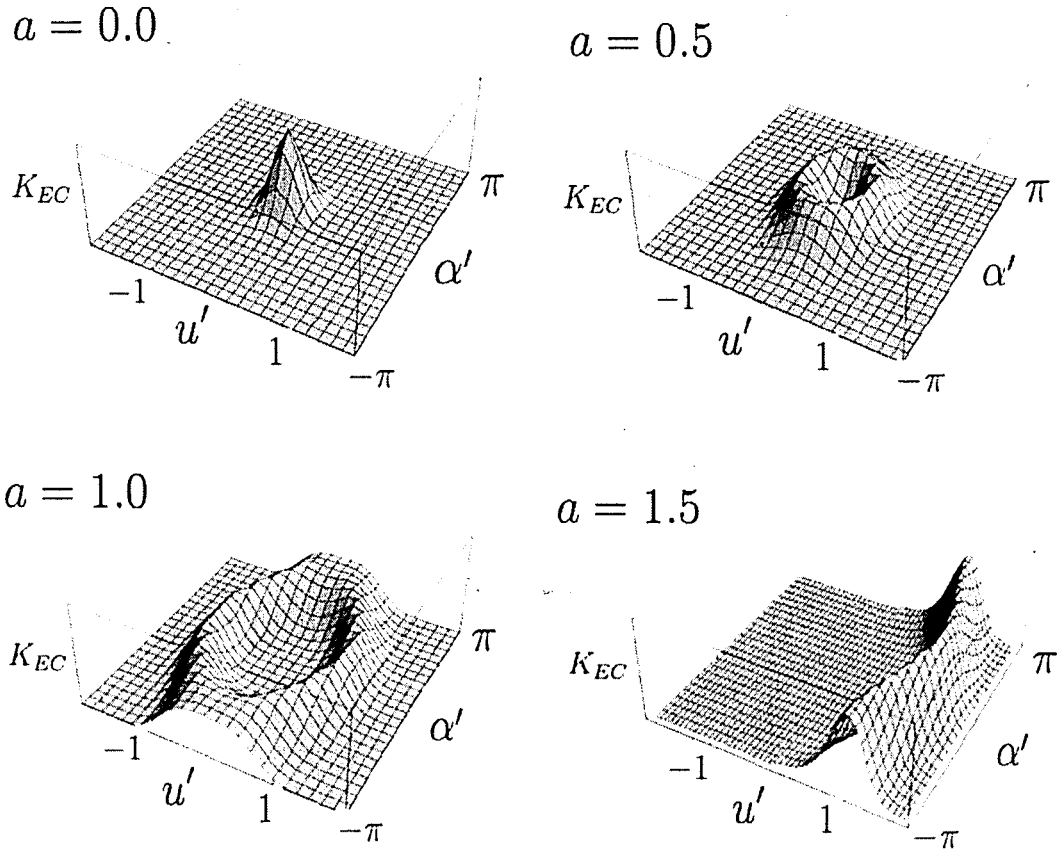

Figure 3.3: Current density after spreading over flux surfaces for various offsets

Chapter 4

Pulsed vs. Continuous Current Drive

As the magnetic islands rotate about the tokamak, it is possible to either pulse the current drive, ideally hitting the islands directly at their center, or "O-point", or leave the current drive on steadily resulting in continuous current drive. First, the somewhat idealized case of current driven entirely at the O-point will be considered, which results in a simplification of the integral (3.4). Then we will consider the continuous drive case, which is experimentally more straightforward.

4.1 Pulsed Current Driven at the O-Point

The integral in Equation (3.4) is complicated because the effects of current spreading over flux surfaces (corresponding to the α' integral) and the effect of island rotation

(which spreads the current drive over angle α at the value of u at which it is driven), are both taken into consideration.

The first simplifying approximation is to assume that the current is driven only near the widest part of the island, near $\alpha = 0$. This makes it possible to set $\cos\alpha = 1$ in Equation (3.4), leaving only the single integral over α'

$$K^0_{EC} = \frac{K_m}{\pi}\left\{\int_0^{\alpha_s} \exp\left[\frac{-1}{2\sigma^2}\left(\pm\sqrt{\frac{1-\cos\alpha+2u^2}{2}} - a\right)^2\right]\left(\frac{dA}{dS}\right)_{in} d\alpha \right.$$
$$\left. + \int_{\alpha_s}^{\pi} \exp\left[\frac{-1}{2\sigma^2}\left(\pm\sqrt{\frac{1-\cos\alpha+2u^2}{2}} - a\right)^2\right]\left(\frac{dA}{dS}\right)_{out} d\alpha\right\} \qquad (4.1)$$

where the prime on the dummy integration variable has been dropped, as well as the prime on the u' of Equation (3.4). The trapezoid rule for computing these integrals numerically is

$$\int_0^{\alpha_s} f(\alpha)d\alpha \approx \frac{\alpha_s}{n}\left[\frac{f(0)+f(\alpha_s)}{2} + \sum_{k=1}^{n-1} f(k\frac{\alpha_s}{n})\right],$$
$$\int_{\alpha_s}^{\pi} f(\alpha)d\alpha \approx \frac{\pi-\alpha_s}{n}\left[\frac{f(\alpha_s)+f(\pi)}{2} + \sum_{k=1}^{n-1} f(\alpha_s + k\frac{\pi-\alpha_s}{n})\right] \qquad (4.2)$$

where n can be increased to give a more accurate approximation.

When performing the integration, it is important to note that inside the island (corresponding to the integration from 0 to α_s), the results will be symmetric in u. Mathematically, this requires taking half the sum of the integrals along positive u, corresponding to the $(+)$ sign in Equation (4.1), and the integral along negative u, corresponding to the $(-)$ sign. Outside the island, the upper $(+)$ sign of Equation (4.1) is used for the outboard island edge and the lower $(-)$ sign is used for the inboard edge.

4.2 Continuous Current Drive

While current drive pulsed at the island O-point is expected to be the most effective technique for shrinking saturated magnetic island widths, it is also useful to consider continuous current drive. Experimentally, it is often easier to implement continuously driven current since magnetic islands rotate helically about the tokamak, making their location difficult to determine in real time.

For continuously driven current, we return to the general double integral of Equation (3.4), without setting $\alpha = 0$ as in the previous section. This double integral is performed numerically by using the trapezoid rule, Equation (4.2), twice. The discussion of the previous section for the sign choice in Equation (3.4) for the outboard (+) and inboard (−) island edges still holds.

Chapter 5

Differential Flux Surface Areas

In the following sections, two different (but related) methods will be presented for finding the differential area term, dA/dS in the integrals (4.1) for pulsed current drive and (3.4) for continuous drive, which will be called "method 1" and "method 2". Another normalization method closely related to method 2 will be referred to as "method 2 - arclengths".

5.1 Method 1

This first differential area approximation is based on the idea that although the Gaussian current is driven at all u-locations, it will have a maximum at a, where it is centered. It also has a characteristic width, given by the variance σ. Outside a width of approximately 2σ, the magnitude of the current drive will be negligible. Therefore, for this method, the differential area in which the current is driven is computed only in a

rectangle of area

$$dA = 2\sigma \times 2\delta\alpha \tag{5.1}$$

where $2\delta\alpha$ is some small extension of the current drive in the angular coordinate, as shown in Figure 5.1. This current, which is applied in the differential area dA, is spread over the region between flux surfaces with area dS. The differential flux surface area dS inside the island can be approximated by the difference of two ellipses, whose semiminor axes differ by 2σ, where σ again is the variance of the Gaussian current drive. The notation a_1 is used for the semiminor axis of the smaller ellipse and a_2 for the semiminor axis of larger ellipse, where $a = (a_1 + a_2)/2$ is the offset of the current drive. Similarly, b_1 denotes the semimajor axis of the smaller ellipse and b_2 that of the larger ellipse. We also define the average $b = (b_1 + b_2)/2$. It is assumed that all the ellipses have the same elongation π, found from the ratio of the angular length of the island ($= 2\pi$) to the width of the island at its widest point ($= 2$). For the ellipses, then

$$\frac{b}{a} \approx \frac{b_1}{a_1} \approx \frac{b_2}{a_2} \approx \pi. \tag{5.2}$$

Noting that the area of the i-th ellipse is given by $\pi a_i b_i$, the differential area between ellipses 1 and 2, dS, is simply

$$dS_{in} = \pi(a_2 b_2 - a_1 b_1) \tag{5.3}$$

$$= \pi^2(a_2^2 - a_1^2) \tag{5.4}$$

$$= \pi^2 \left[(a_2 - a_1)(a_2 + a_1)\right] \tag{5.5}$$

$$= \pi^2 \left[(2\sigma)(2a)\right] \tag{5.6}$$

$$= 4\pi^2 \sigma |a| \tag{5.7}$$

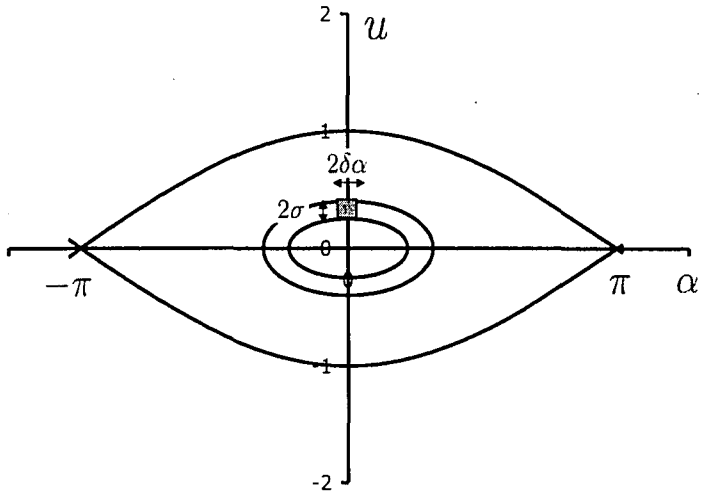

Figure 5.1: Normalization methods 1 and 2

where the absolute value was used since the normalization is independent of the sign of a, and the area element is always positive. Equations (5.1) and (5.7) lead to the result

$$\left(\frac{dA}{dS}\right)_{in} \approx \frac{\delta\alpha}{\pi^2|a|} \tag{5.8}$$

for $|a| > \sigma$. A simple way to generalize this result is to use

$$\left(\frac{dA}{dS}\right)_{in} \approx \frac{\delta\alpha}{\pi^2 \text{Max}\left[|a|, \sigma\right]}. \tag{5.9}$$

Outside the island, it is assumed that flux lines are approximately straight. The applied current area is the same, $dA_{out} = 2\sigma \times 2\delta\alpha$, and $dS_{out} = 2\sigma(2\pi)$. This leads to the approximation

$$\left(\frac{dA}{dS}\right)_{out} \approx \frac{\delta\alpha}{\pi} \tag{5.10}$$

But dS_{out} will be somewhat larger near the island edge, since the flux surfaces are not straight there but slightly curved. To make the results continuous at $|a| = 1$, the

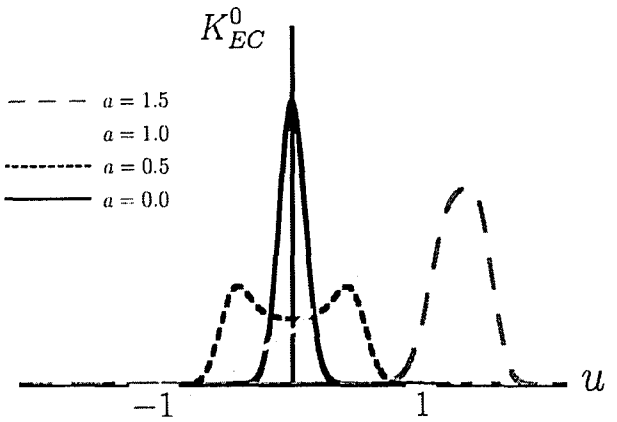

Figure 5.2: Method 1, $\sigma = .1$, $\delta\alpha = 0.1$, arbitrary peak value

following approximation is used

$$\left(\frac{dA}{dS}\right)_{out} = \frac{\delta\alpha}{\pi^2}. \tag{5.11}$$

Using these approximations for the normalization produces the results for the axisymmetric averaged current drive, K^0_{EC}, shown in Figure 5.2 for pulsed current drive with $\sigma = 0.1$ and $\delta\alpha = 0.1$. The scale on the vertical axis of Figures 5.2, 5.4, 5.5, 5.6, 5.7, and 5.8 is arbitrary and therefore not shown — but this scale is kept equal throughout so results are comparable.

To use these ratios of differential flux surface areas for continuous current drive the width of the drive is set to $\delta\alpha = \pi$.

5.2 Method 2

The second method uses the entire current drive profile instead of using only the portion of the current drive near the peak of the Gaussian to compute dA/dS. As before, it is assumed that current is driven over a finite angular range $2\delta\alpha$. The current that is deposited sufficiently close to the O-point of the magnetic island, over flux surfaces with a "major axis" smaller than $2\delta\alpha$ has $dA/dS = 1$. The boundaries of this region that has $dA/dS = 1$ will be discussed further below. Outside this region, but still within the island, taking a difference in areas of ellipses as in method 1, but using u instead of a as the semiminor axis in Equation (5.8),

$$\left(\frac{dA}{dS}\right)_{in} = \frac{\delta\alpha}{\pi^2|u|}. \tag{5.12}$$

For continuity at the island edge (at $|u| = 1$) the following normalization is chosen outside the island

$$\left(\frac{dA}{dS}\right)_{out} = \frac{\delta\alpha}{\pi(1+\frac{\pi-1}{u^2})} \tag{5.13}$$

In Equations (5.12) and (5.13), u is the radial coordinate of a given flux surface at $\alpha = 0$. At any other location on the flux surfaces over which the current is spread, u has to be replaced by the expression given in Equation (2.12), which results in the following expressions

$$\left(\frac{dA}{dS}\right)_{in} = \frac{\sqrt{2}\delta\alpha}{\pi^2\sqrt{1+2u^2-\cos\alpha}} \tag{5.14}$$

$$\left(\frac{dA}{dS}\right)_{out} = \frac{\delta\alpha}{\pi\left[1+\frac{2(\pi-1)}{1+2u^2-\cos\alpha}\right]} \tag{5.15}$$

where the prime on u has been dropped for consistency with the dummy integration variable of equations (3.4) and (4.1).

The region that is sufficiently close to the island O-point and therefore has $dA/dS = 1$ is bounded by the flux surface $\delta\alpha(u)$ shown in Figure 5.3. The "X-point" of this flux surface is given by $\delta\alpha(u = 0) \equiv \delta\alpha$, *i.e.* the extension of the current drive in the angular coordinate. At $\alpha = 0$, the flux surface $\delta\alpha(u)$ crosses the u-axis at two points $\pm u^*$ in Figure 5.3. Expressions for $\delta\alpha(u)$ and u^* can be found from the relationship between u, u', and α' when $\alpha = 0$, Equation (2.12). Since $\delta\alpha(u' = 0) = \delta\alpha$, the point u^* is found by setting $u' = 0$, $\alpha' = \delta\alpha$ in Equation (2.12),

$$u^* = \sqrt{\frac{1 - \cos(\delta\alpha)}{2}} \tag{5.16}$$

where $\delta\alpha$ is a constant. Now, since $\delta\alpha(u) = u^*$ at $\alpha = 0$, Equation (2.12) can also be used to show that

$$u^* = \sqrt{\frac{1 + 2u^2 - \cos[\delta\alpha(u)]}{2}} \tag{5.17}$$

Rearranging, and generalizing the expression, the flux surface $\delta\alpha(u)$ can be described by

$$\delta\alpha(u) = \cos^{-1}\left(\min\left[1, |1 + 2u^2 - 2u^{*2}|\right]\right) \tag{5.18}$$

Inside this flux surface, the area ratio $dA/dS = 1$.

The averaged current drive density can be found separately in the region where u is close to zero and outside this region. All the current driven near the island center, in the region near $u = 0$, $\alpha = 0$, will remain there, and $dA/dS = 1$. But outside this region $dA/dS \neq 1$, and the normalization terms from Equations (5.12) and (5.13) must be

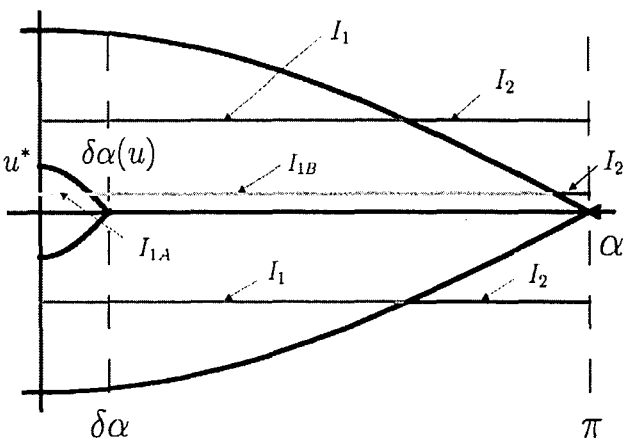

Figure 5.3: Integration paths for normalization method 2

used. As shown in Figure 5.3, the axisymmetric averaged current drive is found as

$$K_{EC}^0 = I_{1A} + I_{1B} + I_2 \qquad |u| < u^* \tag{5.19}$$

$$K_{EC}^0 = I_1 + I_2 \qquad |u| > u^* \tag{5.20}$$

where

$$I_1 = \frac{1}{\pi}\int_0^{\alpha_s}\left(\frac{dA}{dS}\right)_{in} K_{EC}(\psi)d\alpha \tag{5.21}$$

$$I_{1A} = \frac{1}{\pi}\int_0^{\delta\alpha(u)} K_{EC}(\psi)d\alpha \tag{5.22}$$

$$I_{1B} = \frac{1}{\pi}\int_{\delta\alpha(u)}^{\alpha_s}\left(\frac{dA}{dS}\right)_{in} K_{EC}(\psi)d\alpha \tag{5.23}$$

$$I_2 = \frac{1}{\pi}\int_{\alpha_s}^{\pi}\left(\frac{dA}{dS}\right)_{out} K_{EC}(\psi)d\alpha \tag{5.24}$$

Recall that in Equation (4.1), (+) denotes integration along positive u, and (−)

is along negative u. Similar to the discussion of method 1, the integration inside the island (integrals I_1, I_{1A}, and I_{1B}), should be independent of the sign of u. Outside the island (I_2), the (+) sign denotes the region outboard of the island, and the (−) sign denotes the inboard region. Taking all this into consideration, and assuming pulsed CD at the island O-point, the integrals I are given by

$$I_{1A} = \frac{K_m}{\pi}\int_0^{\delta\alpha(u)} \left\{ \exp\left[\frac{-1}{2\sigma^2}\left(+\sqrt{\frac{1+2u^2-\cos\alpha}{2}} - |a|\right)^2\right] + \exp\left[\frac{-1}{2\sigma^2}\left(-\sqrt{\frac{1+2u^2-\cos\alpha}{2}} - |a|\right)^2\right]\right\} d\alpha \quad (-u^* < u < u^*) \tag{5.25}$$

$$I_{1B} = \frac{K_m \delta\alpha}{\pi^3}\int_{\delta\alpha(u)}^{\alpha_s} (1+2u^2-\cos\alpha)^{-1/2} \left\{ \exp\left[\frac{-1}{2\sigma^2}\left(+\sqrt{\frac{1+2u^2-\cos\alpha}{2}} - |a|\right)^2\right] + \exp\left[\frac{-1}{2\sigma^2}\left(-\sqrt{\frac{1+2u^2-\cos\alpha}{2}} - |a|\right)^2\right]\right\} d\alpha \quad (-u^* < u < u^*) \tag{5.26}$$

$$I_1 = \frac{K_m \delta\alpha}{\sqrt{2}\pi^3}\int_0^{\alpha_s} (1+2u^2-\cos\alpha)^{-1/2} \left\{ \exp\left[\frac{-1}{2\sigma^2}\left(+\sqrt{\frac{1+2u^2-\cos\alpha}{2}} - |a|\right)^2\right] + \exp\left[\frac{-1}{2\sigma^2}\left(-\sqrt{\frac{1+2u^2-\cos\alpha}{2}} - |a|\right)^2\right]\right\} d\alpha \quad (-1 < u < -u^* \text{ and } u^* < u < 1) \tag{5.27}$$

$$I_{2+} = \frac{K_m \delta\alpha}{\pi^2}\int_{\alpha_s}^{\pi} \left(1 + \frac{2(\pi-1)}{1+2u^2-\cos\alpha}\right)^{-1} \exp\left[\frac{-1}{2\sigma^2}\left(+\sqrt{\frac{1+2u^2-\cos\alpha}{2}} - a\right)^2\right] d\alpha \quad (u > 0) \tag{5.28}$$

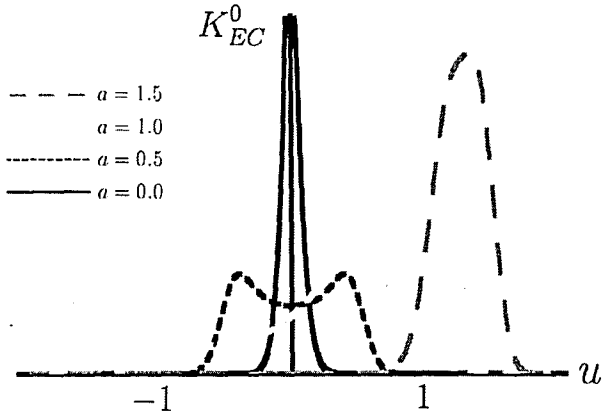

Figure 5.4: Method 2, $\sigma = .1$, $\delta\alpha = 0.1$, same scale and peak value as Figure 5.2

$$I_{2-}=\frac{K_m\delta\alpha}{\pi^2}\int_{\alpha_s}^{\pi}\left(1+\frac{2(\pi-1)}{1+2u^2-\cos\alpha}\right)^{-1}\exp\left[\frac{-1}{2\sigma^2}\left(-\sqrt{\frac{1+2u^2-\cos\alpha}{2}}-a\right)^2\right]d\alpha$$

$(u<0)$ (5.29)

These integrals can be computed numerically, and then combined for the total axisymmetric averaged current drive. The results are illustrated in Figure 5.4 for a narrow pulsed current drive with $\sigma = 0.1$ and $\delta\alpha = 0.1$.

5.3 Comparing Methods 1 and 2

For the parameters presented above, $\sigma = 0.1$ and $\delta\alpha = 0.1$, the two normalization methods produce very similar results, which can be seen by comparing Figure 5.2 with Figure 5.4. The results are not as similar for wider current drives, *i.e.* for larger values of σ. With $\sigma = .5$ we have the results shown in Figure 5.5.

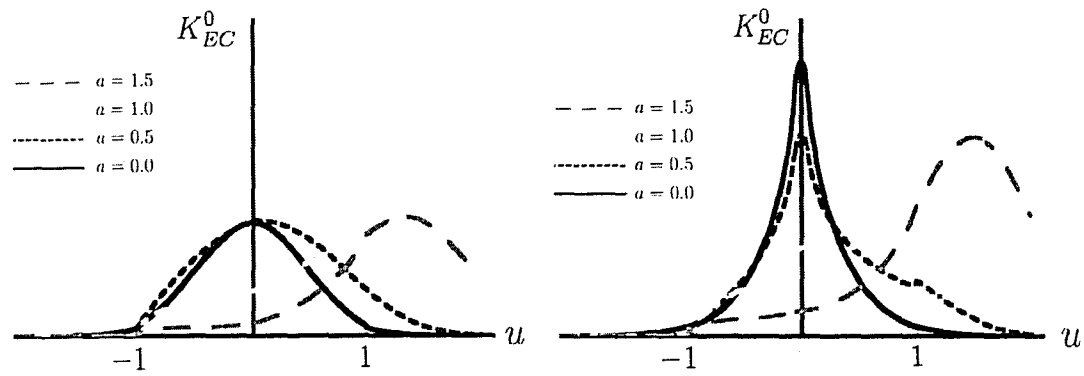

Figure 5.5: Comparing methods 1 (left) and 2 (right), $\sigma = .5$, $\delta\alpha = 0.1$, same peak value

It is important to mention that the first normalization method, "Method 1" is much simpler to implement and produces satisfactory, physically reasonable results. The second method is more rigorous in its derivation, but the results have discontinuities in the derivative of the axisymmetric averaged current drive density. Consequently, normalization "Method 2" is not necessarily an improvement upon the simpler "Method 1". In fact, Method 2 produces a current density peak near $u = 0$ where none should exist for wider current drive ($\sigma = 0.5$), as seen in Figure 5.5.

With any choice of approximation for dA/dS, an important check is whether total current is conserved. The total current applied I_{tot} is proportional to I, where

$$I = \delta\alpha \int_{-\infty}^{\infty} K_{EC} du \tag{5.30}$$

For I to be conserved,

$$\delta\alpha \int_{-\infty}^{\infty} K_{EC} du = \int_{-\infty}^{\infty} \int_{-\pi}^{\pi} K_{EC}(\psi) d\alpha du$$
$$= 2\pi \int_{-\infty}^{\infty} K_{EC}^{0}(u) du \tag{5.31}$$

The results for the right-hand side of Equation (5.31) are presented in Table 5.1 for pulsed current drive with $\delta\alpha = 0.1, \sigma = 0.1, K_m = 1/(\sigma\sqrt{2\pi}) = 3.99$. Since the original Gaussian current drive is normalized, the left-hand side of Equation (5.31) is equal to $\delta\alpha = 0.1$. From this table, it can be seen that current is not conserved in the derivation for either normalization method. This discrepancy has to do with the approximations made in both cases, namely, the assumption that all the closed flux surfaces are ellipses and flux surfaces outside islands are straight lines. These approximations do not hold near the island edge. Further approximations were made for current driven near the island center. These approximations lead to discrepancies of up to a factor of 2 from the expected value in Table 5.1.

	a=0	a=0.5	a=1	a=1.5
Method 1	.051	.069	.102	.074
Method 2	.051	.069	.110	.118

Table 5.1: Total current integrals for $\delta\alpha = 0.1, \sigma = 0.1, K_m = 3.99$

To ensure that the total current is in fact conserved, a "renormalization" factor (simply a constant) is implemented in the ISLAND module.

Methods 1 and 2 have also been compared for other choices of $\delta\alpha$. Figure 5.6 shows the results for $\sigma = 0.5, \delta\alpha = 0.4$.

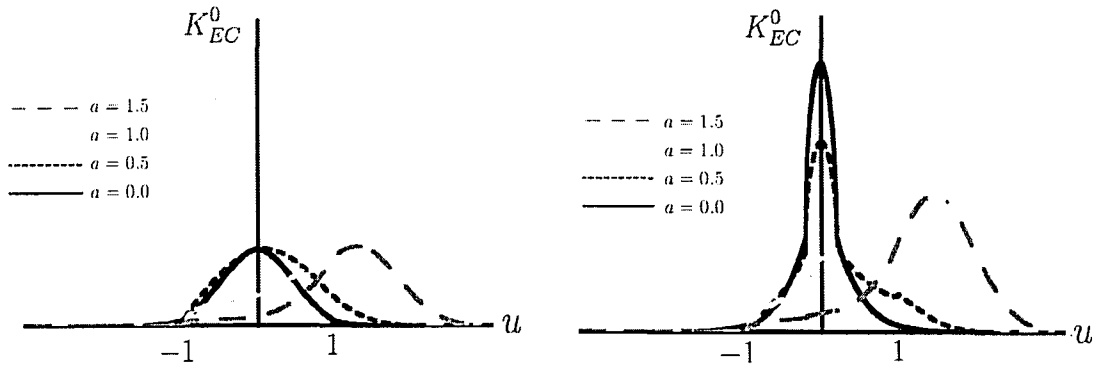

Figure 5.6: Comparing methods 1 and 2, $\sigma = .5$, $\delta\alpha = 0.4$, same total current

5.4 Method 2 - Arclengths

Revisiting method 2, an alternative to using the ratio of areas dA/dS would be to use the ratio of arc lengths. This leads to

$$\begin{aligned}\frac{dA}{dS}_{\text{arc,in}} &= \frac{\sqrt{\frac{5}{2}}\pi\delta\alpha}{2\pi\sqrt{\frac{1}{2}\left(\arccos^2(-2u^2+\cos\alpha)+\frac{1+2u^2-\cos\alpha}{2}\right)}} \\ &= \frac{\sqrt{5}\delta\alpha}{\sqrt{\arccos^2(\cos\alpha-2u^2)+\frac{1+2u^2-\cos\alpha}{2}}} \end{aligned} \tag{5.32}$$

Outside of the island, the normalization has a form similar to that used in method 2 but with a multiplier that is adjusted to produce continuity at $u = 1$

$$\frac{dA}{dS}_{\text{arc,out}} = \frac{5\delta\alpha}{\pi\left[1+\frac{2(\pi-1)}{1+2u^2-\cos\alpha}\right]}. \tag{5.33}$$

Results for this normalization method are shown in Figure 5.7 and 5.8 for narrow and wide current drive shapes, respectively.

Since the results for normalization methods 1, 2, and 2 - arclengths are all quite

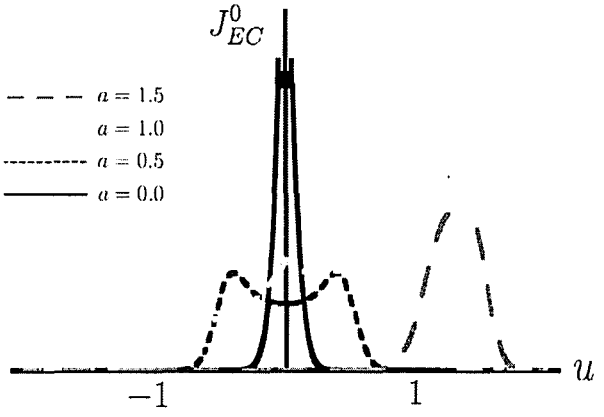

Figure 5.7: Method 2 using arclengths, $\sigma = .1$, $\delta\alpha = .1$, same scale and peak value as Figures 5.2 and 5.4

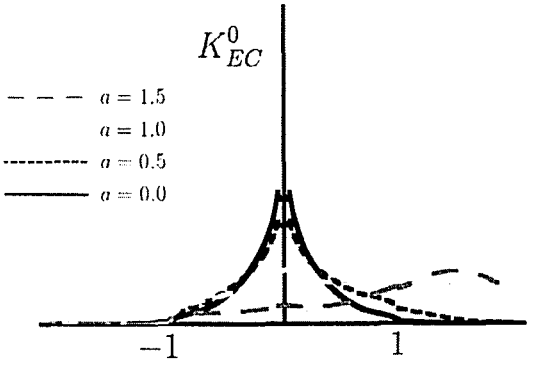

Figure 5.8: Method 2 using arclengths, $\sigma = .5$, $\delta\alpha = .1$, same scale and peak value as Figure 5.5

similar, as can be seen by comparing Figures 5.2, 5.4, and 5.7, or by comparing Figure 5.5 with 5.8, only method 1 was implemented in the ISLAND module.

Chapter 6

Computing the Total Driven Current in Amperes

6.1 Conversion to Real, Physical Units

In practice, the physical current drive parameters (offset a_{real}, width σ_{real}, and magnitude $K_{m,\text{real}}$) are given in units of length (m) and current density (A/m^2), respectively. Therefore it is important to show how to convert from the real, physically relevant units to the more convenient normalized units used in previous sections. As defined previously, a and σ are in u-units (i.e. they are dimensionless), where u is the normalized radial coordinate defined in Equation (2.12). From this, the conversion from the

unitless a to a_{real} in meters is given by

$$a = \frac{1}{H_{mn}} a_{\text{real}} \tag{6.1}$$

$$\sigma = \frac{1}{H_{mn}} \sigma_{\text{real}} \tag{6.2}$$

where H_{mn} is the half-width of the magnetic island in meters.

For the current density peak K_m, the conversion depends on the input current. Since the NTCC ISLAND module comes with two test input files, input_JET and input_DIIID [7], only these will be considered here. The units of K_m as used by the code are 1/m. This is equivalent to the "current peaking factor" in [9]. This current peaking factor and K_m have units of $\mu_0 J/B$, where J and B are the toroidal current density and magnetic field, respectively. Since, for a given input, the magnetic field is constant, $K_{m,\text{real}}$ in A/m^2 is converted to K_m using the average input current. The input current profiles are shown in Figure 6.1, and the conversion is summarized in Table 6.1.

	K_m	$K_{m,\text{real}}$
JET	1 (1/m)	2.336×10^6 (A/m^2)
DIIID	1 (1/m)	1.59155×10^6 (A/m^2)

Table 6.1: Conversion of K_m to real units

6.2 Current Peaking Factor Method — Applied Current

It is of interest to compare results obtained by the procedure outlined in this paper to those obtained from implementation of a "current peaking factor" presented in reference [9]. The current peaking factor method allows for parabolic current peaking through the widest part of the island. It is centered at the island center in the radial direction, with zero current outside the island. The current is driven entirely at $\alpha = 0$ in this case, so the driven current density is represented by

$$K_C = C(1-u^2)\delta(\alpha) \tag{6.3}$$

where $\delta(\alpha)$ is the Dirac delta function and C is the current peaking factor (Note: C has units of 1/rad. The code uses $K = \mu_0 J/B$, which is in units of 1/rad, and J has units of A/m*rad). To convert to physical units of (A/m*rad), multiply by $1/\mu_0 B$, *i.e.*

$$K_{C,\text{real}} = C(1-u^2)\delta(\alpha)\left(\frac{1}{\mu_0 B}\right) \tag{6.4}$$

The total current in Amperes is then found by integrating over u (the normalized radial coordinate) and α (the normalized angular coordinate). To undo the radial normalization, also multiply by the halfwidth H_{mn}

$$\begin{aligned} I_{tot} &= H_{mn} C \left(\frac{1}{\mu_0 B}\right) \int_{-\infty}^{\infty}\int_{-\infty}^{\infty}(1-u^2)\delta(\alpha)\,du\,d\alpha \\ &= H_{mn} C \left(\frac{1}{\mu_0 B}\right) \int_{-\infty}^{\infty}(1-u^2)\,du. \end{aligned} \tag{6.5}$$

6.3 Gaussian Current Drive — Applied Current

The current drive in the ISLAND module code is given by Equation (3.2). The units of K_{EC} are 1/rad, as are the units of K_C. To convert to real units for the applied current drive density, multiplication by $1/\mu_0 B$ is necessary

$$K_{EC,\text{real}} = K_m \exp\left[\frac{-(u-a)^2}{2\sigma^2}\right]\left(\frac{1}{\mu_0 B}\right). \tag{6.6}$$

For the total current in Amperes the expression is integrated over u and α times the halfwidth H_{mn}. The integral over α is just a constant $\delta\alpha$, since the same current is applied over this small angular region. The result is

$$I_{tot} = H_{mn}\delta\alpha K_m \left(\frac{1}{\mu_0 B}\right)\int_{-\infty}^{\infty} \exp\left[\frac{-(u-a)^2}{2\sigma^2}\right] du. \tag{6.7}$$

6.4 Current After Spreading — Current Peaking Factor

After spreading over flux surfaces, the average current drive is given by the integral

$$K^0 = \frac{1}{2\pi}\int_{-\pi}^{\pi} K(\psi) d\alpha. \tag{6.8}$$

For the parabolic current peaking factor method the current density and total current are given by

$$K_C(\psi) = C\left[1 - u^2(\psi)\right] \tag{6.9}$$

$$K_{C,\text{real}}(\psi) = C\left(\frac{1}{\mu_0 B}\right)\left[1 - u^2(\psi)\right] \tag{6.10}$$

$$\begin{aligned} I_{tot} &= H_{mn} C \left(\frac{1}{\mu_0 B}\right) \int_{-\pi}^{\pi} \int_{-\infty}^{\infty} \left[1 - u^2(\psi)\right] du d\alpha \\ &= \frac{2\pi H_{mn}}{\mu_0 B} \int_{-\infty}^{\infty} K_C^0 du. \end{aligned} \tag{6.11}$$

6.5 Current After Spreading — Gaussian

Similarly, for the Gaussian drive, the current density and total current are

$$K_{EC}(\psi) = K_m \exp\left[\frac{-(u(\psi) - a)^2}{2\sigma^2}\right] \tag{6.12}$$

$$K_{EC,real}(\psi) = K_m \left(\frac{1}{\mu_0 B}\right) \exp\left[\frac{-(u(\psi) - a)^2}{2\sigma^2}\right] \tag{6.13}$$

$$\begin{aligned} I_{tot} &= H_{mn} K_m \left(\frac{1}{\mu_0 B}\right) \int_{-\pi}^{\pi} \int_{-\infty}^{\infty} \exp\left[\frac{-(u(\psi) - a)^2}{2\sigma^2}\right] du d\alpha \\ &= \frac{2\pi H_{mn}}{\mu_0 B} \int_{-\infty}^{\infty} K_{EC}^0 du. \end{aligned} \tag{6.14}$$

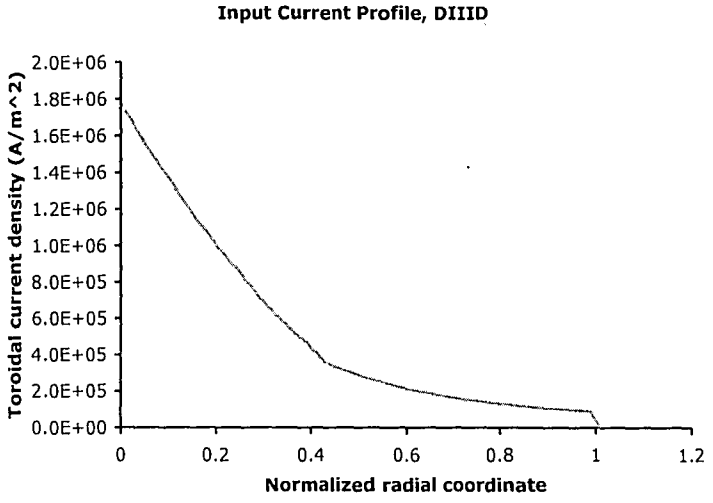

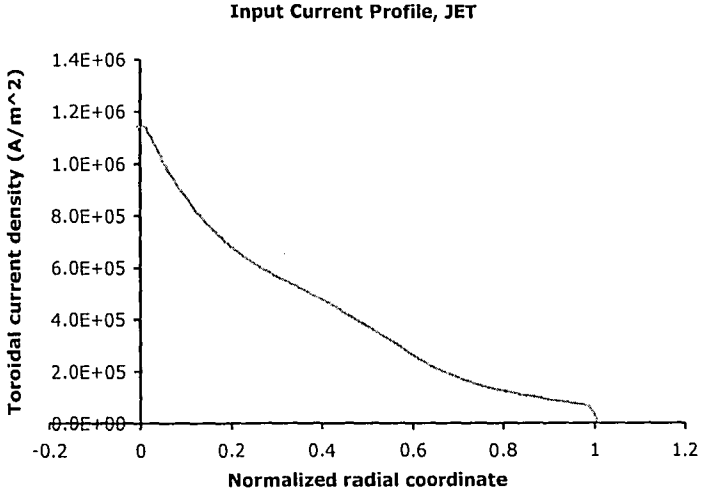

Figure 6.1: Sample input current profiles

Chapter 7

Results from the ISLAND Module

7.1 Results for Pulsed Current Drive

Results for the change in the island width produced by current drive computed using the ISLAND module are shown in Figures 7.1-7.4. These results are for 2/1 islands only. In each plot, the island width is normalized by the plasma minor radius.

In Figure 7.1, the island width as a function of driven current is shown for a pulsed Gaussian current drive profile with $\sigma = 0.3$, $a = 0$, and for parabolic current peaking. The maximum driven current corresponds to about 20% of the background plasma current. In both cases, higher levels of total driven current shrink the island to lower saturated widths. The curves for the pulsed Gaussian and the parabolic current drive

profiles are similar, as is to be expected for a centered Gaussian of equal current. This figure also shows a slight leveling off of the island width for large current drive. As mentioned in Section 1.2, the neoclassical tearing mode is linearly stable, which means that below a certain critical width, magnetic islands will continue to shrink on their own. The ISLAND module is not valid for these small island widths, which helps to explain the leveling of the curves in Figure 7.1.

Figure 7.2 shows the effect of changing the width of the pulsed Gaussian current drive with zero offset, or equivalently, changing the variance of the Gaussian, σ, while fixing the offset at $a = 0$. It can be seen that narrow current drive (small σ) is more effective at shrinking the island, as the slope is more negative in this case. For large current drive width ($\sigma = 1$), much of the driven current falls outside the island, and this portion can have a destabilizing effect, leading to the small slope of the curve with large σ seen in Figure 7.2.

Figure 7.3 shows the effect of changing the current drive center relative to the island center. Here the width of the Gaussian is fixed at $\sigma = 0.4$, and the offset a is varied. The centered current drive is most effective at shrinking the island, and off-center current drive eventually becomes destabilizing. The destabilizing effect is greater for current driven on the inboard side of the island (for negative a) than on the outboard side (positive a).

The island width is plotted as a function of pulsed driven current for a choice of different offsets in Figure 7.4, and the results are as expected. The slope of the saturated island width curve is most negative for centered ($a = 0$) drive, and flattest for $a = 1$.

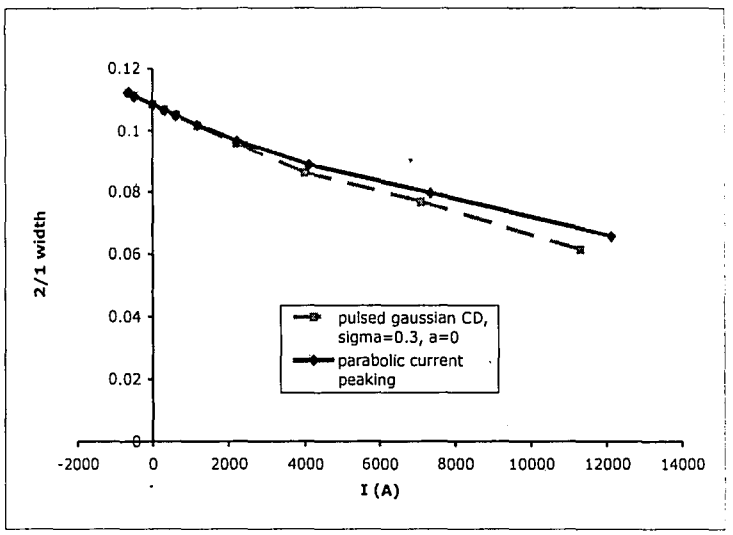

Figure 7.1: Saturated island width vs. total driven current for parabolic current peaking factor (solid) and pulsed Gaussian current drive with $\sigma = 0.3$ and $a = 0$ (dashed)

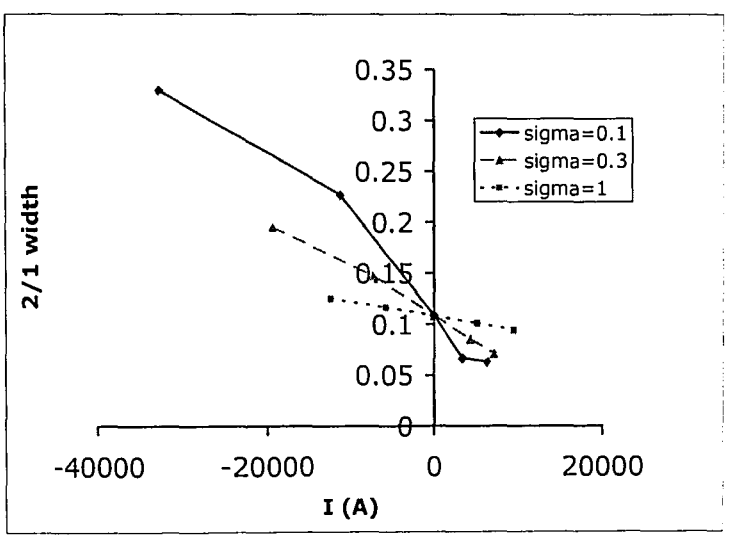

Figure 7.2: Saturated island width vs. total driven current for centered, pulsed Gaussian current drive of different widths

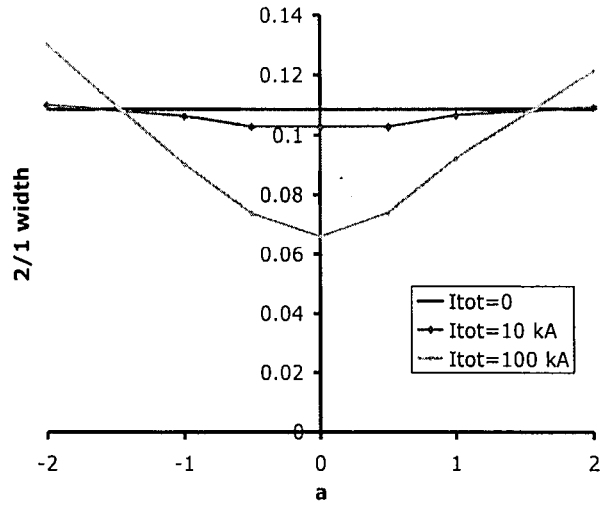

Figure 7.3: Saturated island width vs. offset for pulsed Gaussian current drive of various (approximate) total current drive levels

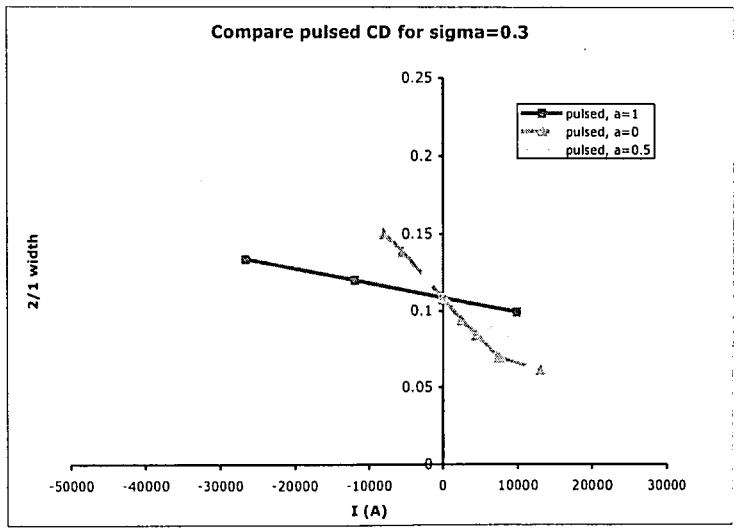

Figure 7.4: Saturated island width vs. driven current for pulsed Gaussian current drive with $\sigma = 0.3$, various offsets

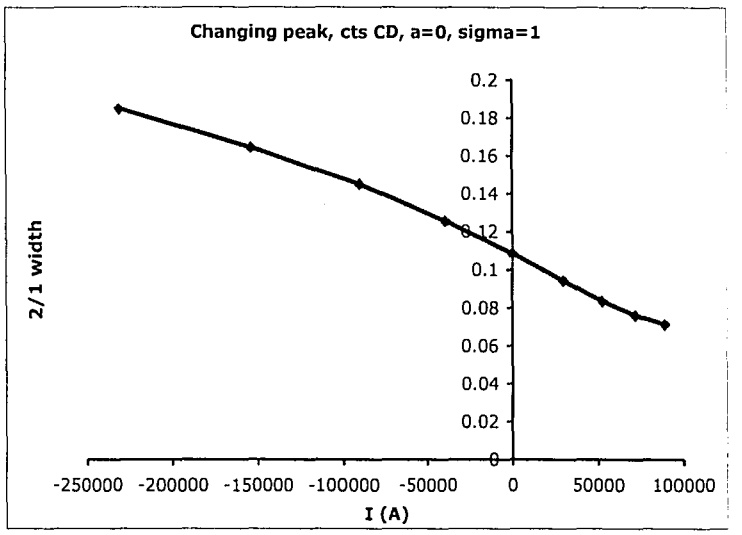

Figure 7.5: Saturated island width vs. total drive current for continuous Gaussian current drive with $a = 0, \sigma = 1$

7.2 Results for Continuous Current Drive in ISLAND

When the continuously driven current is implemented in the ISLAND module, many expected relationships between the current drive shape and the saturated island widths are obtained. Qualitatively, the results are similar to those presented in the previous section for pulsed current drive.

In the case of zero offset current ($a = 0$), for example, with a width on the order of the island width ($\sigma = 1$), it is found that the saturated island width shrinks as the total driven current (as governed by the peak K_m) increases. This relationship is shown in Figrue 7.5.

When the total driven current is held constant, along with zero offset ($a = 0$), a narrower current drive profile is expected to be more effective in shrinking the islands.

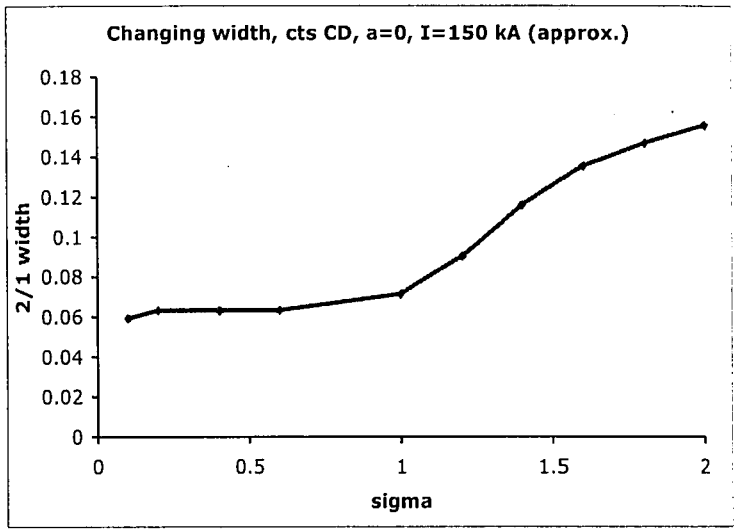

Figure 7.6: Saturated island width vs. continuous Gaussian current drive width σ, $a = 0$, $I_{tot} \approx 1.5 \times 10^5$ A

This behavior is found, although the relationship is not linear, as shown in Figure 7.6.

For a constant level of driven current where both the peak K_m and the width σ are held fixed, a centered current drive is most effective at shrinking the islands. This is shown for different levels of total continuously driven current in Figure 7.7. Figure 7.7 also shows that outboard current drive (positive a) is more stabilizing than inboard drive, as we have seen before. Also, for large offsets, current drive is destabilizing for continuous current drive, as it was for pulsed current drive.

Similarly to Figure 7.4, the island width is plotted as a function of continuous driven current for various offsets in Figure 7.8. Again, the slope of the curve is most negative for centered ($a = 0$) Gaussian current drive, indicating that this current drive profile is most stabilizing. When the offset of the continuous current drive is on the order of the

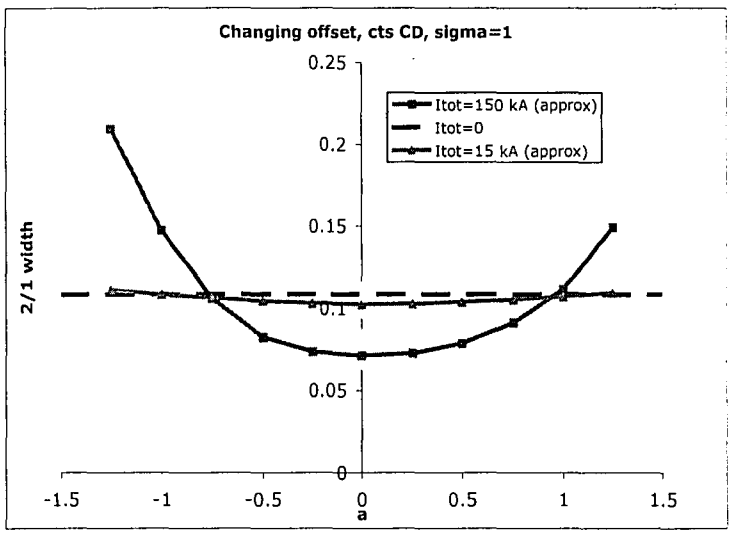

Figure 7.7: Saturated island width vs. offset a for continuous Gaussian current drive, $\sigma = 1$, I_{tot} varies

island width, positive current drive becomes destabilizing, as indicated by the positive slope of the $a = 1$ curve in the positive current region of Figure 7.8.

7.3 Comparing Pulsed and Continuous Current Drive

The previous two sections illustrated many of the qualitative similarities between current drive that is pulsed at the angle of the island O-point and current drive that is on continuously. More quantitative comparisons are presented in this section.

Perhaps the most relevant question to experimentalists is which type of current drive profile is more efficient at shrinking the islands. For a given amount of total current, is it better to pulse the current drive entirely at the angle of the island O-point, or to to leave it on continuously as the islands rotate about the tokamak?

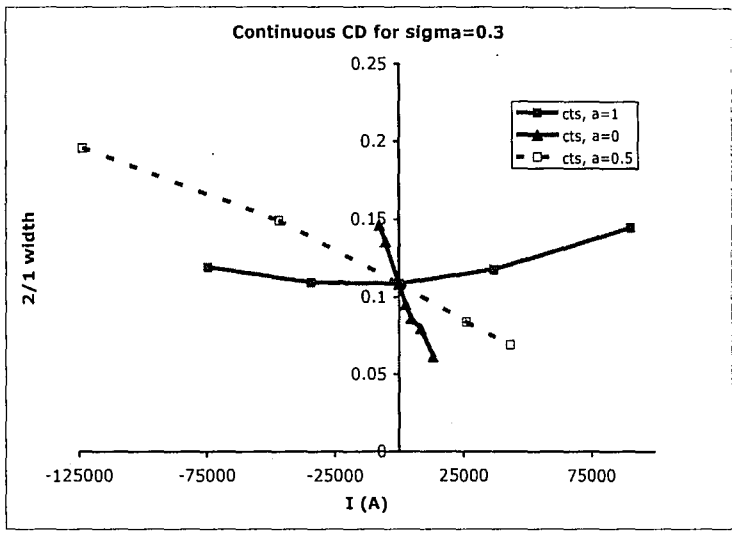

Figure 7.8: Saturated island with vs. total drive current, continuous Gaussian current drive

The island width computed by the ISLAND module is plotted as a function of the driven current in Figure 7.9 for pulsed Gaussian current drive and continuous Gaussian current drive. This figure also shows the results for the original current peaking factor, which represents a pulsed parabolic current drive entirely within the island. As shown before, this parabolic pulsed current drive is quite similar to the Gaussian pulsed current drive. It can be seen in Figure 7.9 that the effect of the continuous Gaussian current drive is nearly the same as the effect of pulsed current drive when both current drive profiles are centered.

Considering a Gaussian current drive that is offset from the island center by half the island width, $a = 0.5$, with the same width $\sigma = 0.3$, produces the results of Figure 7.10. Now the results are very different for pulsed and continuous current drives. It can

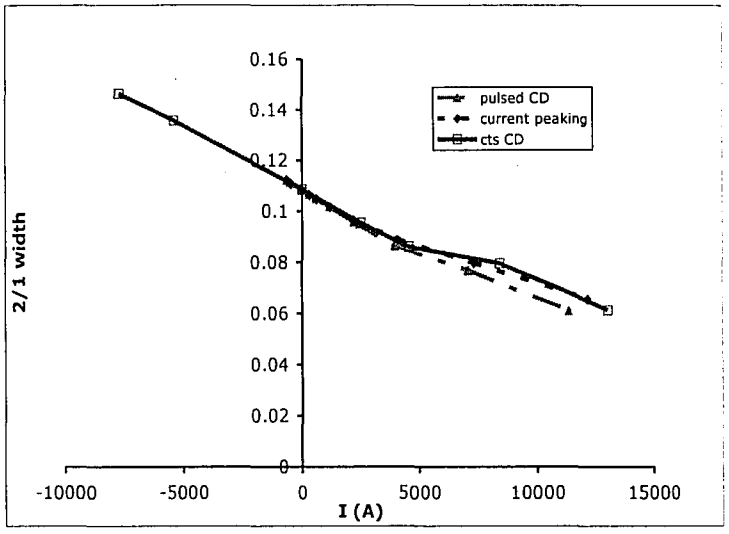

Figure 7.9: Saturated island width vs. total driven current for parabolic, pulsed ($a = 0$, $\sigma = 0.3$), and continuous ($a = 0$, $\sigma = 0.3$) current drive profiles

be seen that the pulsed current drive is much more effective at shrinking the island for this case, as the slope of the curve is more negative.

Increasing the offset of both drives to $a = 1$ exaggerates this effect further, as shown in Figure 7.11. Here, for the same width $\sigma = 0.3$, the pulsed current drive still stabilizes the magnetic island for positive current, while the continuous drive is destabilizing.

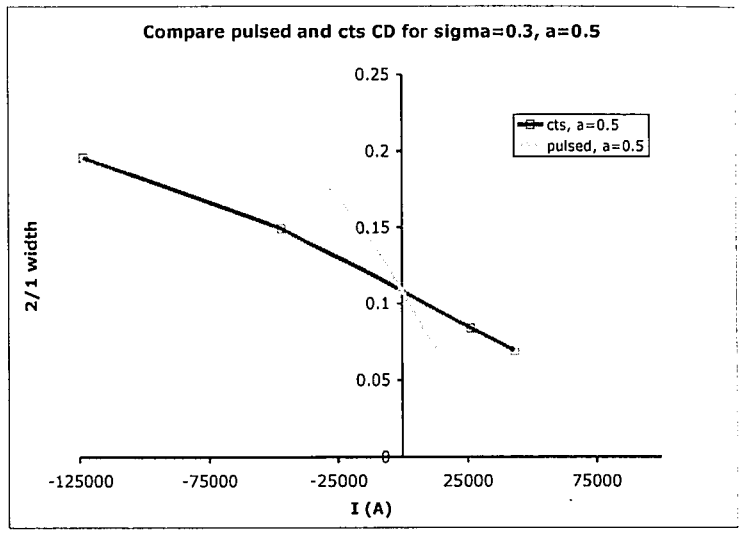

Figure 7.10: Saturated island width vs. total driven current for pulsed and continuous current drive profiles, $a = 0.5$, $\sigma = 0.3$

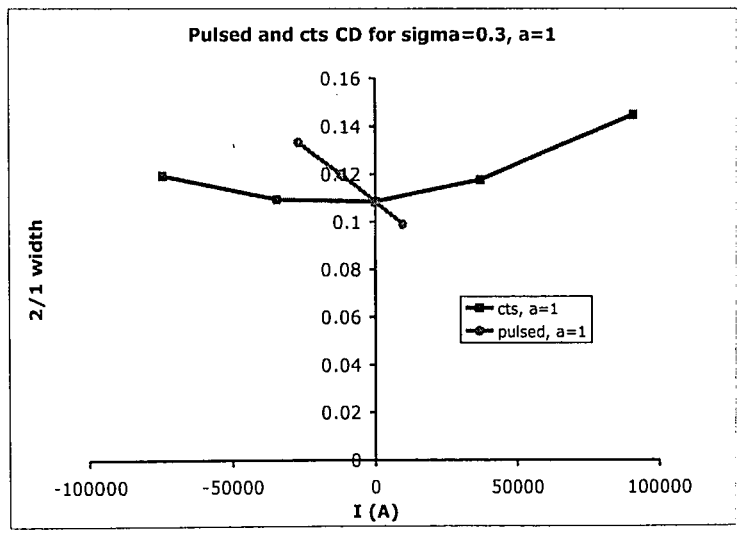

Figure 7.11: Saturated island width vs. total driven current for pulsed and continuous current drive, $a = 1$, $\sigma = 0.3$

Chapter 8

Conclusions

A model for localized current drive for stabilization of the neoclassical tearing mode instability has been developed and implemented in the ISLAND module as a pulsed current drive (driven at the angle of the island O-point), and as a continuously driven current. Simulations with various pulsed current drive profiles have demonstrated that the current drive model produces results similar to those obtained from a centered parabolic current peaking when the total current and current drive shape were similar. For both pulsed and continuous current drive, it was shown that when the current drive is radially centered on the island, narrow current drive profiles are more efficient at shrinking the magnetic islands than wide current drive profiles in which much of the driven current falls outside the island. It was also shown that when the current drive width is held fixed, current drive profiles that are radially centered at the island center shrink the islands more than current drive profiles that are offset from the island center. For current drive offsets from the island center that are large relative to the island

width, the effect of positive current drive is destabilizing. For both pulsed and continuous current drive, this destabilizing effect is stronger for current driven at the inboard island edge rather than the outboard edge.

Comparing the pulsed current drive with the continuous drive, results indicate that the pulsed CD is more effective at shrinking the island for equal amounts of total current. This result is expected, since current pulsed at the island O-point injects far more current into the island, and less outside.

Implementation of current drive in the ISLAND module provides the foundation for future work studying the stabilization of the neoclassical tearing mode instability computationally. These simulation results are consistent with experimental results. Results indicate that a radially centered current drive will have the strongest stabilizing effect, represented by a local minimum on a plot of saturated magnetic island width as a function of current drive offset. This minimum lends itself particularly well to extremum seeking control, for which the location of the island need not necessarily be known. Such a control algorithm would represent an improvement over current "search-and suppress" algorithms.

Bibliography

[1] C. Hegna and J. Callen, "On the stabilization of neoclassical magnetohydrodynamic tearing modes using localized current drive or heating," *Physics of Plasmas*, vol. 4, pp. 2940–2946, 1997.

[2] R. Buttery, S. Gunter, G. Giruzzi, T. Hender, *et al.*, "Neoclassical Tearing Modes," *Plasma Phys. Control. Fusion*, vol. 42, pp. B61–B73, 2000.

[3] R. La Haye, "Neoclassical tearing modes and their control," *Physics of Plasmas*, vol. 13, p. 055501, 2006.

[4] D. Humphreys, J. Ferron, R. La Haye, *et al.*, "Active control for stabilization of neoclassical tearing modes," *Physics of Plasmas*, vol. 13, p. 056113, 2006.

[5] N. Hayashi, T. Ozeki, K. Hamamatsu, *et al.*, "ECCD power necessary for the neoclassical tearing mode stabilization in ITER," *Nuclear Fusion*, vol. 44, pp. 477–487, 2004.

[6] G. Giruzzi, M. Zabiego, T. Gianakon, *et al.*, "Dynamical modelling of tearing mode stabilization by RF current drive," *Nuclear Fusion*, vol. 39, pp. 107–125, 1999.

[7] F. Halpern, G. Bateman, A. Kritz, and A. Pankin, "The ISLAND module for computing magnetic island widths in tokamaks," *J. Plasma Physics*, vol. 72, pp. 1153–1157, 2006.

[8] F. Halpern, G. Bateman, and A. Kritz, "Integrated simulations of saturated neoclassical tearing modes in DIII-D, JET, and ITER plasmas," *Physics of Plasmas*, vol. 13, p. 062510, 2006.

[9] G. Bateman and R. Morris, "Saturated tearing modes in toroidal geometry," *Physics of Fluids*, vol. 29, pp. 753–761, 1986.

[10] R. Morris, "Ph.D. thesis," *Georgia Inst. of Technology*, 1984.

[11] C. Nguyen, G. Bateman, and A. Kritz, "Simulation of saturated tearing modes in tokamaks," *Physics of Plasmas*, vol. 11, pp. 3460–3471, 2004.

Vita

Jennifer Woodby was born in Landstuhl, Germany on August 3, 1982. She completed the Abitur at St. Franziskus Gymnasium in Kaiserslautern, Germany in 2002. Later that year she entered Princeton University and earned a Bachelor of Arts degree with honors in Physics in 2006. She began work toward a Master of Science degree in Mechanical Engineering at Lehigh University in the fall of 2006.

END OF TITLE